ACS Sustainable Chemistry & Engineering

pubs.acs.org/journal/ascecg

Research Article

Effect of O_2 on Plasma-Based Dry Reforming of Methane: Revealing the Optimal Gas Composition via Experiments and Modeling of an Atmospheric Pressure Glow Discharge

Stein Maerivoet,* Bart Wanten,* Robin De Meyer, Morgane Van Hove, Senne Van Alphen, and Annemie Bogaerts

Cite This: *ACS Sustainable Chem. Eng.* 2024, 12, 11419−11434

Read Online

ACCESS | Metrics & More | Article Recommendations | Supporting Information

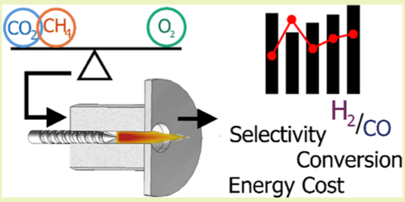

ABSTRACT: Plasma technology is gaining increasing interest for the conversion of greenhouse gases, such as CO_2 and CH_4, into value-added chemicals using (renewable) electricity. In this paper, we study the effect of O_2 addition to the combined conversion of CO_2 and CH_4 in an atmospheric pressure glow discharge plasma. This process is called "oxidative CO_2 reforming of methane", and we search for the optimal gas mixing ratio in terms of conversion, energy cost, product output and plasma stability. A mixing ratio of 42.5:42.5:15 $CO_2/CH_4/O_2$ yields the best performance, with a CO_2 and CH_4 conversion of 50 and 74%, respectively, and an energy cost as low as 2 eV molecule^{-1} (corresponding to 7.9 kJ L^{-1} and 190 kJ mol^{-1}), i.e., clearly below the target defined to be competitive with other technologies. The syngas components (CO and H_2) are the most important products, with a syngas ratio, H_2/CO, being 0.8. Plasma destabilization at high CH_4 fractions due to solid carbon formation is the limiting factor for further improving this syngas ratio. The solid carbon material is found to be contaminated with steel particles originating from the electrode material, rendering it unappealing as a side product. Therefore, O_2 addition helps to remove the carbon formation. Besides the experiments, we developed a 2D axisymmetric fluid dynamics model, which can successfully predict the experimental trends in conversion, product composition and temperatures, while providing unique insights in the formation of C_xH_y species.

KEYWORDS: *plasma-based conversion, thermal plasma, syngas production, CO_2 conversion, CH_4 conversion*

1. INTRODUCTION

Due to global warming, there is an urgent need for the conversion of CO_2 and CH_4 into value-added chemicals or fuels. The basic reaction is known as the dry reforming of methane (DRM)

$$CH_4\ (g) + CO_2\ (g) \rightarrow 2CO\ (g) + 2H_2\ (g) \quad \Delta H^0 = +247\ \text{kJ mol}^{-1}$$

Theoretically this reaction should give a conversion of 100% at 1500 K. An optimal energy efficiency of 70% is reached at 1000 K, with a conversion of 83%.[1] This reaction produces syngas, a mixture of H_2 and CO, theoretically in a 1:1 ratio (at an equal conversion of both reactants, with the latter also supplied in a 1:1 ratio).

At higher temperatures, however, the above reaction is accompanied by side reactions, such as the reaction of CO_2 with H_2, known as the reverse water−gas-shift reaction, which has a lower reaction enthalpy[2]

$$CO_2\ (g) + H_2\ (g) \rightarrow CO\ (g) + H_2O\ (g) \quad \Delta H^0 = +41.1\ \text{kJ mol}^{-1}$$

Such side reactions make the preferred conversion of CO_2 and CH_4 into syngas more difficult, producing lower-value side products.

Syngas is an important mixture of reactants for the production of small organic compounds in the chemical industry, e.g., for the production of methanol, formaldehyde and for the Fischer−Tropsch process to create carbon-neutral fuels and lubricants.[2,3] Different syngas ratios are optimal for producing different organic compounds. For example, a syngas ratio (H_2/CO) of 2 is optimal for the Fischer−Tropsch process when using a cobalt catalyst.[4] However, the optimal ratio can vary between 1.7 and 2.15,[5] and when using an iron catalyst, lower syngas ratios (around 1) are also suitable.[6] Also for the production of methanol, a ratio of 2 is ideal, which enables a "methanol economy"[7] for its higher energy density compared to H_2, its use in polymer chemistry and the usage of the direct methanol fuel cell.[7,8]

Received: May 24, 2024
Revised: July 1, 2024
Accepted: July 2, 2024
Published: July 15, 2024

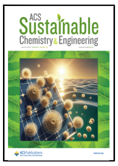

https://doi.org/10.1021/acssuschemeng.4c04283
ACS Sustainable Chem. Eng. 2024, 12, 11419−11434

Many technologies are being investigated for CO_2 and CH_4 conversion.[1] One of the novel technologies gaining increasing interest, is plasma technology. Plasma is a partially (or fully) ionized gas, containing charged species, as well as radicals and exited species exhibiting a collective behavior. Radicals and highly energetic electrons provide a way toward otherwise impossible reaction pathways, which makes a plasma reactor an interesting tool for the conversion of thermodynamically stable molecules, such as CO_2 and CH_4.[9]

Plasma operates by applying electricity, and can immediately be turned on/off at ambient conditions. This gives plasma reforming an advantage when working with green energy sources. When excess energy is available, it can be used by plasma reactors to create value-added chemicals. Therefore, plasma creates an ideal pathway for chemical energy storage, providing an attractive alternative for large batteries.

Plasma-based DRM has already been extensively studied in various plasma types, showing promising results. A detailed literature overview of all plasma types was provided in 2017 by Snoeckx and Bogaerts,[1] and was updated in 2022 by Wanten et al.[10] While a lot is known already, a few challenges remain defiant for plasma-based DRM to mature as a technology. The energy efficiency of this processes has to be comparable or better than current technologies. Buttler and Spliethoff report the energy efficiency of electrolysis for energy storage of green hydrogen to be between 60 and 80%, which is a direct competition for the industrialization of plasma-based DRM.[11] Hence, optimization of the reactor design, plasma conditions and experimental mixtures is needed to compete with the industry standard. On the other hand, DRM has the advantage that the produced gas is immediately accessible for further chemical processes, such as the Fischer−Tropsch process, without the need of supplying additional CO or CO_2 similar to producing syngas with electrolysis.[12]

While the steam reforming of methane (SRM) is a viable alternative to DRM, combining CH_4 and H_2O, classical SRM suffers from its own downsides. This reaction is carried out at high temperatures (1023−1223 K) and elevated pressures (14−20 atm) on a Ni/Al_2O_3-catalyst bed, but suffers from deactivation of the catalyst due to coking and sintering of Ni particles.[13]

Wanten et al. used an atmospheric pressure glow discharge (APGD) plasma reactor for DRM, and were able to convert 64% of CO_2 and 94% of CH_4, at an energy cost of 3.5−4 eV molecule^{-1}.[10] However, the authors reported a second major challenge facing plasma-based DRM, namely the on-time of the plasma was severely limited by solid carbon formation. Indeed, CH_4 can also react without CO_2, as described for example by the Kassel mechanism, where CH_4 is converted into small hydrocarbons (which are also detected experimentally in this work), and they are subsequently decomposed into H_2 and solid carbon.[14] This is problematic, as excessive carbon formation affects the plasma conductivity, making the plasma unstable, and it can even extinguish the plasma completely. Solid carbon formation highly depends on the CH_4/CO_2 ratio, which therefore has to be limited for the reactor to operate without excessive solid carbon formation. This limits the reachable syngas ratio of the plasma system, voiding the advantage of immediately using the plasma products as reagents for other chemical processes, like the Fischer−Tropsch process.

The problem of solid carbon formation can be solved by adding O_2 to the gas mixture, allowing the following reaction to oxidize the carbon material[15]

$$\text{C (s)} + \text{O}_2\text{ (g)} \rightarrow \text{CO}_2\text{ (g)} \qquad \Delta H^0 = -393.5\ \text{kJ mol}^{-1}$$

We hypothesize that adding O_2 can also affect the formed syngas ratio, because it may allow to use a higher CH_4 fraction without destabilizing the plasma. Hence, in the present study, we investigate O_2 addition to a CO_2/CH_4 mixture in an APGD plasma reactor. This process is called "oxidative CO_2 reforming of methane" (OCRM). Our main goal is diminishing solid carbon formation, which should allow us to use higher fractions of CH_4, aiming to obtain a higher syngas ratio.

To understand the underlying physics and chemistry and to evaluate the predictability of our experiments, we also developed a fluid dynamics model. The temperature in this APGD reactor is above 2000 K, and many plasma species are very reactive and short-lived, making measurements of species densities or core temperatures in an optically blocked plasma reactor, due to the ceramic piece, very complicated. Therefore, modeling can provide unique insights into the physics and chemistry, such as reaction pathways. Specifically, we developed a 2D axisymmetric model to calculate the temperature profile and gas flow behavior in the reactor, self-consistently coupled with the plasma chemistry.

2. EXPERIMENTAL & COMPUTATIONAL DETAILS

2.1. cAPGD Reactor. We use a so-called confined APGD (cAPGD) reactor, which was designed to yield superior performance compared to a basic APGD reactor.[16] It consists of a cathode pin and anode plate, and the space in-between is encapsulated by a ceramic tube. The latter makes sure that the plasma is filling most of the reactor, and thus all the gas is passing through the plasma.[16] Both cathode pin and anode plate are made of Therma 310S stainless steel, ensuring heat and reasonable corrosion resistance against high plasma temperatures and deterioration by energetic plasma species.[16] The ceramic tube is made of MACOR, being sufficiently heat-resistant against the nearby plasma.[17] Figure 1 shows the position and dimensions of the cathode, anode and ceramic tube, and also illustrates the flow lines in the reactor.

The ceramic tube encapsulates the cathode pin exactly, resulting in a high vortex flow through the grooves (±1 mm deep) of the cathode grooves. The high vortex flow results in flow cooling of the cathode and cathode tip, and thus limits melting of the latter.[16] The flow leaves the cathode grooves touching the ceramic tube, ensuring a high flow cooling of the ceramic tube wall as well. Both effects allow for a

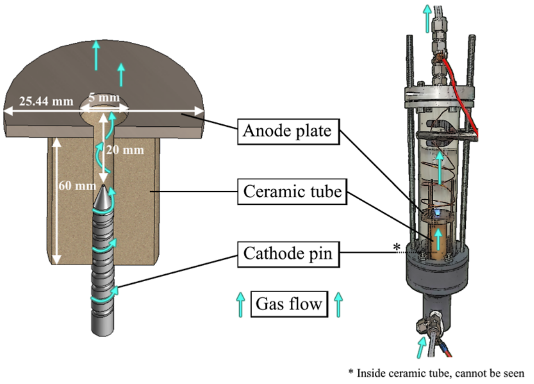

Figure 1. Schematic representation of the cAPGD, with indication of the position of cathode, anode and ceramic tube, the characteristic dimensions, and the direction of the gas flow (turquoise arrows).

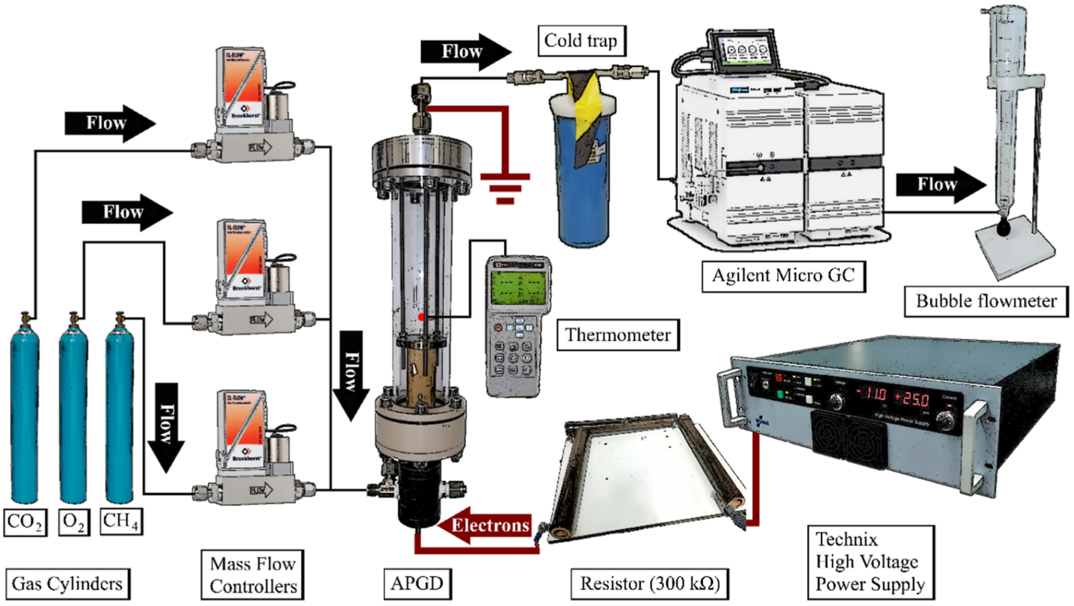

Figure 2. Schematic representation of the entire experimental setup. Black thin lines depict gas flow; red thick lines depict electrical current.

Table 1. Overview of All the Experimental Conditions

	series A					
$CO_2/CH_4/O_2$ (%/%/%)	65:35:0	62:34:3	61:33:6	59:32:9	57:31:12	55:30:15
plasma power (W)	85 ± 6	97 ± 5	97 ± 5	97 ± 5	95 ± 5	93 ± 5
input flow rate (L min^{-1})	1.04 ± 0.01	1.07 ± 0.02	1.04 ± 0.01	1.05 ± 0.01	1.04 ± 0.01	1.04 ± 0.01
	series B					
$CO_2/CH_4/O_2$ (%/%/%)	55:30:15	49:36:15	42.5:42.5:15	36:49:15		
plasma power (W)	93 ± 5	95 ± 5	94 ± 5	75 ± 6		
input flow rate (L min^{-1})	1.04 ± 0.01	1.04 ± 0.01	1.06 ± 0.02	1.05 ± 0.01		

higher power to be used in comparison with a basic APGD reactor, where there is no confinement of the plasma, and this higher power is beneficial for the conversion.[16]

2.2. Experimental Setup. Figure 2 schematically illustrates the entire experimental setup. Gas flow (thin black lines) is provided by three 99.9% purity, © Air Liquide gas cylinders: CO_2, CH_4 and O_2. These gases pass through their respective Bronkhorst mass flow controllers (MFC) and are mixed to be sent to the APGD through the flow channel of the cathode pin, as shown in Figure 1. After exiting the plasma and leaving the reactor, the resulting gas mixture enters an ice-filled cold trap, condensing all products with low boiling points to liquid form. The cold trap is necessary to avoid entrance of any liquid samples to the Agilent micro gas chromatograph (μGC), which would cause severe damage. The gas exiting the cold trap is further led toward the GC as a homogeneous mixture. For each measurement, either plasma or blank, the GC has a sample period of 30 s, extracting gas flow from the setup, after which it is injected onto the column. Details on the μGC are given in the Supporting Information, Section S.1.1. After a gas sample is injected onto the GC columns, the gas passes through without any flow loss and the exact flow rate is measured using a bubble flow meter.

Before the plasma is turned on, a blank measurement is performed, obtaining GC data on the real concentrations in the inlet gas mixture. Simultaneously, the exact output flow rate is measured using a bubble flow meter. The flow rate measured during a blank measurement is equal to the flow rate at the inlet of the reactor during a plasma measurement. Both the concentrations and measured flow rates are used to calculate performance metrics such as conversion and product selectivity, as described in more detail in the Supporting Information, Section S.1.2. Correction factors for gas expansion due to the reaction of DRM are taken into account, as also explained by Pinhão et al.[18] and Wanten et al.[19] The details are provided in the Supporting Information, Section S.1.3.

As mentioned above, a cold trap is used to condense all products with low boiling points. This liquid fraction is analyzed by a Thermo Focus SSL GC with Stabilwax column and FID, as explained in the Supporting Information, Section S.1.4, and is mainly H_2O. As H_2O cannot be detected in the GC, its concentration formed in the plasma is based on the O atom-balance, as also explained in the Supporting Information, Section S.1.4.

The electrical circuit is marked by thick dark red lines in Figure 2. A high voltage DC power supply [Technix HV (SR30KV-1.2KW)] is set at a current of 25 mA and 30 kV and is used to ignite the plasma. This power supply is grounded through the power inlet. The generated current flows through a resistor of 300 kΩ toward the APGD, where the charge accumulates at the tip of the cathode pin before igniting. The potential difference between the cathode pin and the grounded anode plate ignites the plasma.

Using thermocouples and a cylindrical glass casing with an extra opening, we could measure the temperature at different locations (although not inside the plasma, due to the hindrance by the ceramic tube, too high temperature for the thermocouples and interference with the plasma itself), i.e., outside the ceramic tube, in the afterglow and at the outlet. Most interesting is the temperature measured in the afterglow, because it yields measurable differences at different conditions; its position is also indicated in Figure 2, i.e., the thermocouple tip is placed approximately 1 cm above the anode.

2.3. Experimental Conditions Investigated. We investigated two experimental series, called A and B. In series A, we increase the O_2 fraction up to 15%, keeping the CO_2/CH_4 ratio fixed. The 15% O_2 fraction is determined as the upper limit, to keep all experiments safe and well below the explosion limit; see more details on the experimental safety precautions in Supporting Information, Section

S.1.5. In series B, we increase the CH_4 fraction, while the CO_2 fraction drops and the O_2 fraction is kept constant at 15%. The exact experimental conditions are listed in Table 1.

The plasma power fluctuates slightly, depending on the initial gas mixture. Indeed, although the initial voltage of the power supply is set to 30 kV, the potential difference drops immediately after ignition, and its value is determined by the reaction conditions themselves. At a constant current, the gas composition and the cathode−anode distance have the largest impact on the voltage, which results in some variation in terms of power over the series of experiments. As the current I and the resistance of the resistor R_{resistor} are known, i.e. 25 mA and 300 kΩ, respectively, and the total voltage V_{total} can be read from the PSU display, the plasma power P_{plasma} can be determined by subtracting the resistor power from the total power

$$P_{\text{plasma}} = P_{\text{total}} - P_{\text{resistor}} = (V_{\text{total}} \times I) - (I^2 \times R_{\text{resistor}}) \tag{1}$$

The total gas inlet flow rate was set at 1 L min^{-1} for all gas mixing ratios, but the measured flow rates are not exactly 1 L min^{-1} due to a systematic error on the MFCs. The flow rates listed in Table 1 were measured using the bubble flow meter depicted in Figure 2. However, despite this systematic error, the deviations between the values are small, just like the error margins on the measured values, indicating that no significant error is introduced when determining the correction factor α (see Supporting Information, Section S.1.3).

2.4. Analyses of Solid Carbon Deposits. When CH_4 is present in the reactant mixture, especially at higher fractions, solid carbon formation is observed. Black particles are deposited on the electrodes, as well as on the walls of the ceramic and the glass of the reactor. Furthermore, the formation of solid carbon also yields a lower plasma stability, hindering operation at elevated CH_4 fractions. In addition, the carbon material may accumulate over time, potentially leading to blockages and contamination of the downstream system, posing significant challenges to long-term operations.

In order to understand the structure of this carbon material, and to investigate whether it may be a valuable side product, we analyzed this material by scanning electron microscopy (SEM) and transmission electron microscopy (TEM). For the SEM analyses, we employed a Thermo Fisher Scientific Quanta FEG 250, which was additionally equipped with an Oxford Instruments energy dispersive X-ray (EDX) detector, enabling spectroscopic analyses to determine the elemental composition of the samples. The TEM measurements were performed using a Thermo Fisher Scientific Tecnai Osiris G20, operated at 200 kV in bright-field (BF) TEM imaging mode. For the SEM analyses, we placed the collected material directly on a double-sided conductive carbon tape. Prior to TEM analyses, the sample was suspended in acetone by sonication and vortexing, after which a few drops of the suspension were placed on a holey carbon TEM grid that was left to dry under ambient conditions.

In addition to the characterization of the formed carbon particulates, we also investigated whether O_2 addition affects the properties of the formed solid carbon material, by analyzing two samples. Each sample was collected at the anode of the reactor after operating the plasma for 1 h in a 36:49:15 $CO_2/CH_4/O_2$ mixing ratio for the "with O_2" sample, and a 65:35:0 mixing ratio for the "without O_2" sample.

2.5. Description of the Fluid Dynamics Model. The model used in this paper was developed by Maerivoet et al.,[20] but applied here to many more experimental conditions (see Table 1), compared to the five conditions studied in the original model paper. We provide only a brief description here, as we use the model only to obtain more insights in the underlying chemistry, but it is not the main focus of this paper. A combination of a 3D gas fluid dynamics model and a 2D coupled gas flow + plasma model is required to obtain realistic results. Specifically, the 3D gas fluid dynamics model feeds an inflow velocity field to the 2D axisymmetric coupled model, since the geometry of the cathode does not allow for an axisymmetric inflow below the cathode (see Figure 1). The 3D model only solves the gas flow equations, i.e., the Reynolds-averaged Navier−Stokes Shear Stress Transport equations, while the 2D axisymmetric coupled model also includes heat balance equations, chemistry and transport of species. Additional details on the 3D simulation can be found in the Supporting Information, Section S.2.

The transport of species equation in the 2D axisymmetric model follows a mixture-averaged model, where this equation describes the conservation of mass[21]

$$\nabla\cdot\left(-\rho D_i^m \nabla\omega_i - \rho\omega_i D_i^m \frac{\nabla M_n}{M_n} + \boldsymbol{j}_{c,i} - \boldsymbol{j}_{T,i}\right) + \rho(\boldsymbol{u}\cdot\nabla)\omega_i = R_i \tag{2}$$

Here, ρ is the gas density, D_i^m is the diffusion coefficient for species i, M_n is the mean molar mass, $\boldsymbol{j}_{c,i}$ is the multicomponent diffusive flux correction term, $\boldsymbol{j}_{T,i}$ is the turbulent diffusive flux vector, $\boldsymbol{u}$ is the gas flow velocity vector, ω_i is the weight fraction of species i, and R_i is the total net production rate of species i. All reaction rate coefficients for the reactions used in the model can be found in the Supporting Information, Section S.3.

A detailed description of the multicomponent diffusive flux correction term and of the turbulent diffusive flux vector, together with the calculation for the diffusion coefficients, can be found in Section S.2 of the Supporting Information or the COMSOL User Guide.[21,22] To solve the 2D model within a reasonable calculation time, the number of species included in this model is 21, and is determined by a reduction and sensitivity analysis, as described by Maerivoet et al.[20]

The conservation of momentum in the 2D model is also described using the Reynolds-averaged Navier−Stokes equations with Menter's SST model describing turbulent flow[23,24]

$$\nabla\cdot(\rho\boldsymbol{u}) = 0 \tag{3}$$

$$\rho(\boldsymbol{u}\cdot\nabla)\boldsymbol{u} = \nabla\cdot\left[-p\boldsymbol{I} + (\mu + \mu_T)(\nabla\boldsymbol{u} + (\nabla\boldsymbol{u})^T) - \frac{2}{3}(\mu + \mu_T)(\nabla\cdot\boldsymbol{u})\boldsymbol{I} - \frac{2}{3}\rho k\boldsymbol{I}\right] \tag{4}$$

Here, p is the gas pressure, $\boldsymbol{I}$ is the unity tensor, μ is the dynamic viscosity, μ_T is the turbulent dynamic viscosity, k is the turbulent kinetic energy, and superscript T describes transposition.

The turbulent kinetic energy, k, used in eq 4, and the specific dissipation rate, ω, are calculated with

$$\rho(\boldsymbol{u}\cdot\nabla)k = \nabla\cdot[(\mu + \mu_T\sigma_k)\nabla k] + P - \beta_0^*\rho\omega k \tag{5}$$

$$\rho(\boldsymbol{u}\cdot\nabla)\omega = \nabla\cdot[(\mu + \mu_T\sigma_\omega)\nabla\omega] + \frac{\gamma}{\mu_T}\rho P - \rho\beta\omega^2 + 2(1 - f_{v1})\frac{\sigma_{\omega 2}\rho}{\omega}\nabla k\cdot\nabla\omega \tag{6}$$

Here P is the turbulent kinetic energy source term, β_0* and $\sigma_{\omega 2}$ are turbulence modeling parameters, γ,β, σ_k and σ_ω are turbulence parameters depending on the blending functions f_{v1} and f_{v2}. Further description of the turbulence equations and the turbulence modeling parameters can be found in the Supporting Information, Section S.2.

The conservation of energy is solved using a modified heat balance equation, which accounts for the transport of species and heat released by chemical reactions[22]

$$\rho C_p\boldsymbol{u}\cdot\nabla T + \nabla\cdot(-(k + k_T)\nabla T) + \sum_i \frac{\bar{H}_i}{M_i}r_i = Q + \sum_i \boldsymbol{j}_i\cdot\nabla\frac{\bar{H}_i}{M_i} \tag{7}$$

Here, C_p is the heat capacity at constant pressure, T is the temperature, k is the thermal conductivity, k_T is the turbulent thermal conductivity, $\bar{H}_i$ is the molar enthalpy of species i, M_i is the molar mass of species i, r_i is the reaction rate of species i, Q is the user-defined heat source, which is the power deposited in the plasma, and $\boldsymbol{j}_i$ is the diffusive flux vector of species i.

We describe the plasma using a heat source, instead of by equations for the current conservation and Poisson equation, to save computation costs. This approximation is valid, as the APGD is quasi-thermal. We use imaging of the APGD plasma by Trenchev et al.[16] to obtain a realistic heat source shape. Boundary conditions and additional in depth description of the modeling equations and geometry can be found in the Supporting Information (Section S.2) and in the paper by Maerivoet et al.[20]

3. RESULTS AND DISCUSSION

3.1. Measured Conversion, Energy Cost, Product Output. *3.1.1. Conversion.* In Figure 3a we plot the conversion of CO_2, CH_4 and O_2, as well as the total conversion, describing the converted fraction of the gas mixture as a whole, as a function of the O_2 fraction in the input mixture (i.e., series A, cf. Section 2.3 above). Every condition is measured in three successive experiments, consisting each of three samples, leading to consistent values and thus small error bars, as shown in Figure 3a. The conversion of all three molecules increases with rising O_2 fraction, and thus the total conversion rises as well.

The higher CH_4 conversion upon rising O_2 fraction can be explained by the partial oxidation of CH_4 with O_2, which means an additional conversion pathway besides DRM, as well as by a higher gas temperature (see Section 3.4.3.). The rising CO_2 conversion is a bit less intuitive. A higher O_2 fraction opens a pathway toward full oxidation of CH_4 into CO_2, which would lead to a net drop of CO_2 conversion. However, O_2 addition leads to a higher gas temperature (see Section 3.4.3 below), because of the energy released by the reaction of O_2 with CH_4; indeed, partial oxidation of CH_4 is an exothermic reaction. This will lead to a higher conversion in general (as the chemistry is mainly driven by thermal reactions at these high temperatures), and thus also the CO_2 conversion. The net effect of these phenomena is a slight increase of CO_2 conversion upon rising O_2 fraction. This trend is more extensively described in the paper by Maerivoet et al.[20]

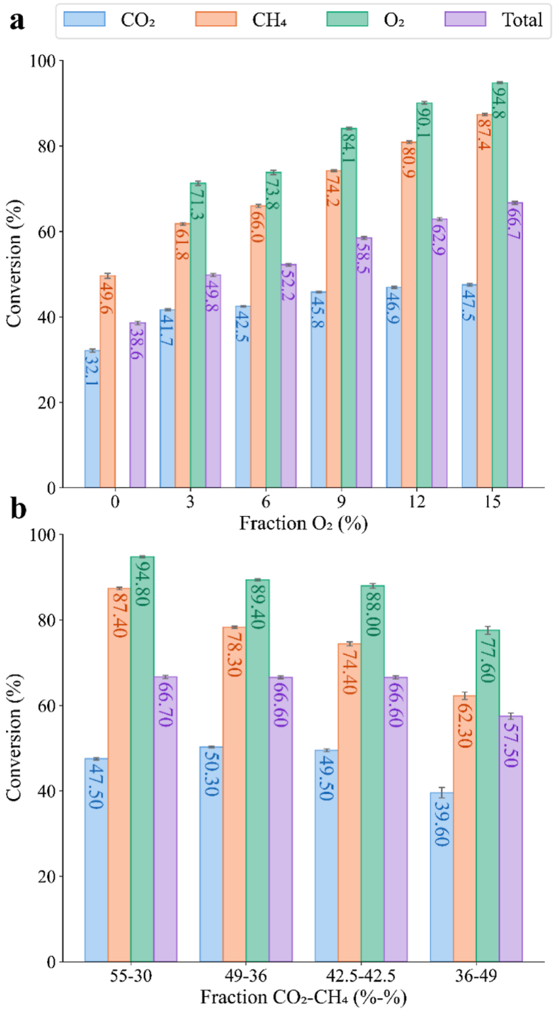

Figure 3. Conversion of CO_2, CH_4 and O_2, as well as the total conversion, as a function of O_2 fraction [(a) series A], and CO_2/CH_4 fraction [(b) series B]. The error bars are based on three successive experiments.

Figure 3b illustrates the conversion of CO_2, CH_4 and O_2, as well as the total conversion, as a function of CO_2/CH_4 fraction in the mixture, at fixed O_2 fraction of 15% (i.e., series B, cf. Section 2.3 above). At the applied current and flow rate, a CH_4 fraction above 49% was not possible, because it creates an unstable plasma due to the formation of too many solid carbon particles inside the plasma, which are further discussed in Section 3.2. The evolution toward an unstable plasma can be observed from the (slightly) increasing error margin at higher CH_4 fractions. The conversions of CH_4 and O_2 both drop upon higher CH_4 fractions. Since the conversion of CO_2 increases slightly upon increasing CH_4 fraction up to the 42.5:42.5:15 $CO_2/CH_4/O_2$ mixture, the total conversion remains around 67% until this mixing ratio, followed by a drop at higher CH_4 fraction.

Hence, we define the 42.5:42.5:15 $CO_2/CH_4/O_2$ mixture as the best condition (also in combination with the results below), yielding a total conversion of 66.6 ± 0.4%, and corresponding CO_2 and CH_4 conversions of 49.5 ± 0.3 and 74.4 ± 0.5%, respectively. This condition does not coincide with the highest CO_2 conversion, which is reached for the 49:36:15 mixture, i.e., 50.3 ± 0.2%.

At the highest O_2 conversion of 94.8 ± 0.2%, reached for the 55:30:15 mixture (see Figure 3a,b), we still have some solid carbon deposits. As almost all O_2 is "used" (converted) in this case, while we also near the safety explosion limit, we should introduce a different oxidizing agent for the solid carbon. The addition of H_2O could be beneficial, as it creates OH radicals, which also destroy solid carbon particles, as observed in a hydrocarbon flame study by Wang et al.[25] We have also recently demonstrated this, in a very similar reactor setup as used in this work.[26]

3.1.2. Energy Cost. Figure 4a depicts the energy cost of series A (i.e., the energy needed to convert 1 molecule of either CH_4 or CO_2), as well as the corresponding plasma power used at each condition. The 65:35:0 $CO_2/CH_4/O_2$ condition operates at a lower power due to the formation of solid carbon at the anode and in the plasma, increasing the plasma conductivity and therefore lowering the power. Since the power remains constant over the rest of the conditions within this series, while the total conversion increases, the energy cost drops. Just like for the conversion, the plasma stability at each condition is again reflected by the magnitude of the error bar. The largest error on the plasma power (for the 65:35:0 condition) represents a change in plasma power over the duration of the experiment. This change is attributed to the formation, destruction and removal by the gas flow of carbon deposits.

Both thermal catalysis and plasma studies show that the carbon in carbon deposits found in DRM originates both from CO_2 and CH_4,[27] although Biswas et al. performed an isotope

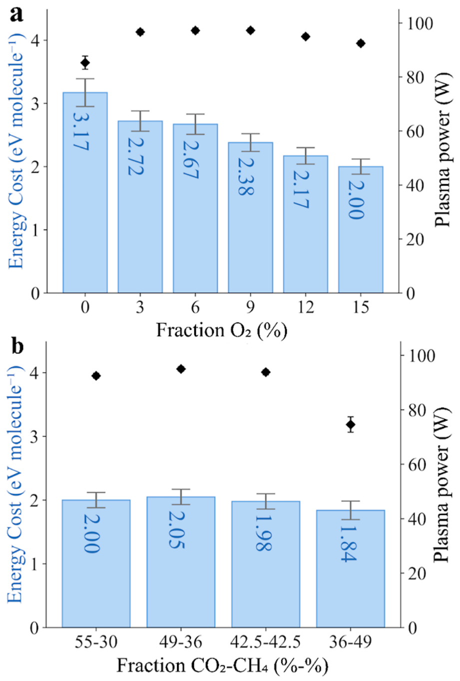

Figure 4. Energy cost in eV molecule^{-1}, as well as plasma power (right y-axis), as a function of O_2 fraction [(a) series A], and CO_2/CH_4 fraction [(b) series B]. Error bars are based on three successive experiments.

labeling study, which suggested that CO production in a DBD plasma operating in CO_2/C_2H_6 primarily originates from CO_2.[28] In fact, Yabe and Sekine discussed the carbon deposits in catalysis not as a function of reactants but as a function of the atomic fractions of each species, where carbon deposits can be avoided as long as enough O is present.[29] Wang et al. discussed the reduction of carbon deposits via OH radicals rather than O radicals, by looking at the addition of H_2O in hydrocarbon flames.[25] This suggestion is in line with our observations of carbon deposits in the APGD DRM plasma. We have analyzed the carbon deposits (see Section 3.2 for the morphology of the solid carbon deposits, and Section 3.4.4 for the pathway analysis).

Furthermore, Biondo et al. studied the effect of the flow dynamics on the formation and destruction of carbon deposits in plasma.[30] It is clear from their research that the physical expulsion of carbon deposits highly depends on the core-periphery transport of the gas. As seen in Figure 1, a vortex flow is present in our APGD, which in turn will result in the removal of some carbon deposits due to physical expulsion. Separating the effect of the physical vs chemical removal of carbon deposits is, unfortunately, not yet possible in our experiments, and thus, beyond the scope of this paper. However, as we keep our flow rate constant at all conditions, we consider that any change in plasma stability is an effect of the changing chemistry, and not because of small differences in the flow regime.

The energy cost of series B (i.e., the energy needed to convert 1 molecule of either CH_4 or CO_2), shown in Figure 4b, is stable across the series. The lowest energy cost of both series is reached at the 42.5:42.5:15 mixture, yielding 1.98 ± 0.12 eV molecule^{-1}, which corresponds to 7.9 ± 0.5 kJ L^{-1} and 190 ± 10 kJ mol^{-1}. The energy cost at the 36:49:15 mixing ratio is even slightly lower (1.84 ± 0.15 eV molecule^{-1}), but this is attributed to the instability of the condition, resulting in a lower measured plasma power. However, this unstable condition also reduces the reproducibility, and therefore we believe the 42.5:42.5:15 mixing ratio is more favorable.

Note that the energy cost plotted in Figure 4 represents the energy cost per converted molecule. The energy cost per produced molecule, i.e., the energy cost of syngas produced, can be found in the Supporting Information, Section S.5. The minimum energy cost of syngas production is also found at condition 36:49:15, reaching 1.28 eV molecule^{-1} of syngas at a 1.07 syngas ratio (see Section 3.1.3). This is due to the drop in the formation of H_2O in series B, while the conversion at this condition is still high (57.5% total conversion).

3.1.3. Syngas Ratio. As illustrated in Figure 5a, the syngas (or H_2/CO) ratio drops upon increasing O_2 fraction. Indeed, the formation of H_2O from CH_4 and O_2 reduces the availability of H for H_2 formation. Note that the trend of how the syngas ratio changes over series A matches the reverse trend of CH_4 conversion in Figure 3a. Indeed, a higher CH_4 fraction in the mixture enhances the H_2/CO ratio, as illustrated in Figure 5b. The best syngas ratio (1.066 ± 0.022) is reached at the 36:49:15 mixing ratio, but the latter has a lower reproducibility (cf. the larger error bar) and also suffers from excessive carbon deposition. Therefore, also in combination with the conversion and energy cost data shown

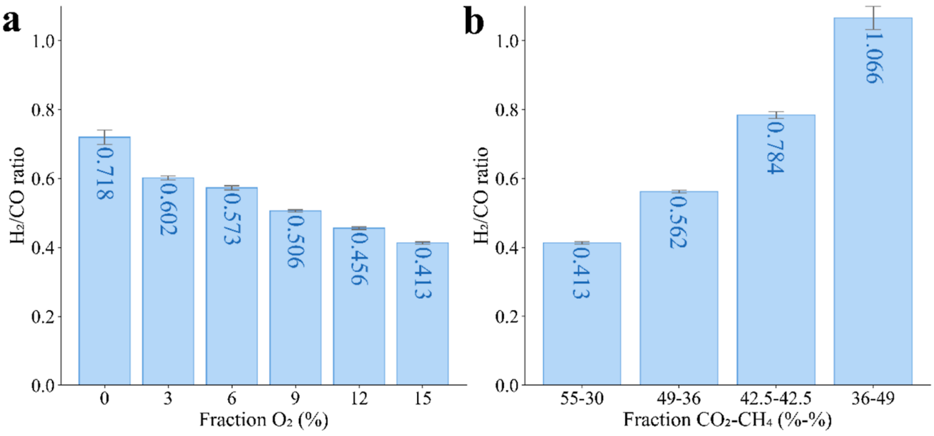

Figure 5. Syngas ratio as a function of O_2 fraction [(a) series A], and CO_2/CH_4 fraction [(b) series B]. Error bars are based on three successive experiments.

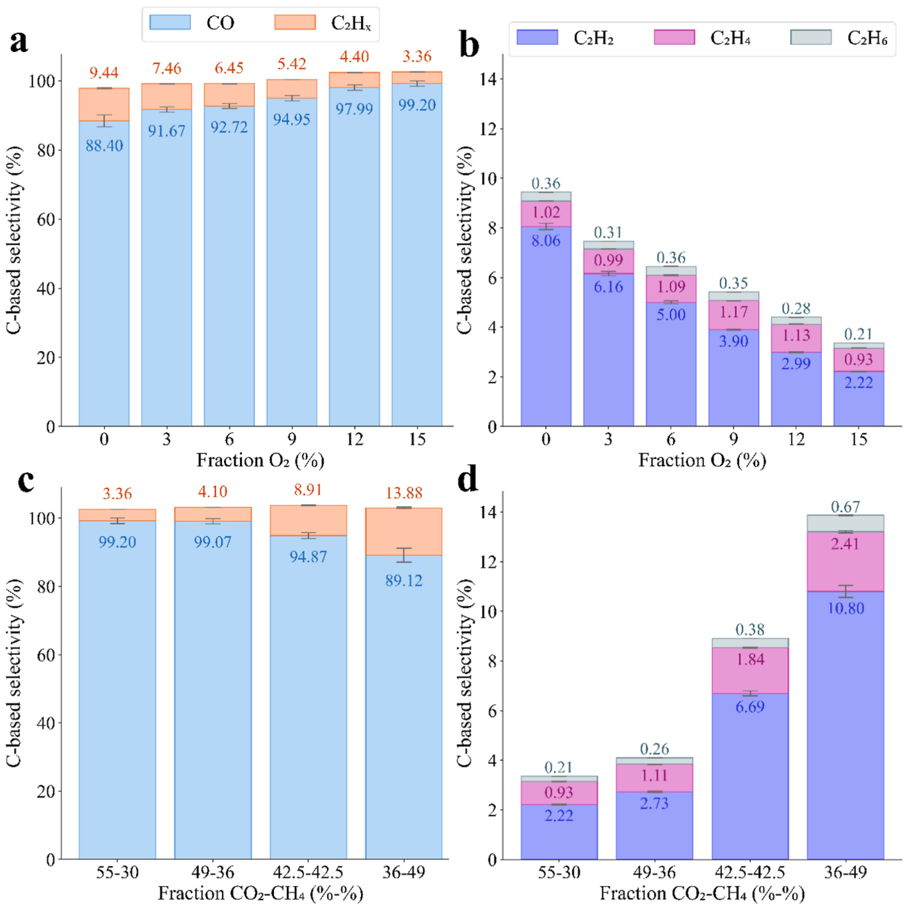

Figure 6. C-based selectivity, as a function of O_2 fraction [(a,b) series A], and CO_2/CH_4 fraction [(c,d) series B]. In (a,c) the C_2H_x compounds are combined, while in (b,d) the individual C_2H_x compounds are shown. Error bars are based on three successive experiments. As the selectivities are calculated from experimental results with small inaccuracies, the total selectivities are not perfectly equal to 1.

above, we believe the 42.5:42.5:15 mixing ratio is more beneficial, in terms of long-term stability due to limited carbon deposition, although it yields a syngas ratio of only 0.784 ± 0.008. This value is too low for most syngas applications, so future work will be focused on further improvements, as will be discussed below. However, as mentioned in the Introduction, the Fischer−Tropsch process with an iron catalyst operates at syngas ratios around 1, making our current results suitable already.[6]

3.1.4. C-Based Product Selectivity. Figure 6a shows the C-based selectivity at each condition of series A, for CO and all C_2H_x molecules together, i.e., C_2H_2, C_2H_4 and C_2H_6. Upon O_2 addition, the CO selectivity rises, while the C_2H_x selectivity drops almost 3-fold, from 9.44 ± 0.14% without O_2 to 3.36 ± 0.02% at 15% O_2 addition. Figure 6b illustrates the C-based selectivity of C_2H_x, split up in its components. The major component is C_2H_2, followed by C_2H_4 and C_2H_6. The highest loss in selectivity with increasing O_2 fraction is therefore attributed to the loss of C_2H_2 selectivity. The C-based selectivity of series B is plotted in Figure 6c. As can be expected, a higher CH_4 fraction leads to a higher C_2H_x selectivity, and the main component is again C_2H_2, as is clear from Figure 6d.

3.1.5. H-Based Product Selectivity. The H-based selectivity of series A is plotted in Figure 7a. Most striking is the rising H_2O selectivity upon increasing O_2 fraction, because the O atoms originating from O_2 react with H from CH_4 dissociation into H_2O, at the expense of H_2 (and C_2H_x) formation. Indeed, both the C_2H_x and H_2 selectivities drop in favor of the H_2O selectivity. The overall larger error bar for the H_2O selectivity is due to the large error on the mass balance. It should be kept in mind that H_2O does not enter the GC and is condensed in a cold trap. The H_2O concentration is determined using the absence of O-atoms when comparing the inlet and outlet mixtures (see Supporting Information, Section S.1.3). Therefore, the H_2O concentration depends on the concentration of every other component, hence, its error will always be larger than any of the directly measured components at the GC. Figure 7b depicts the evolution of C_2H_x components over series A, demonstrating a drop in C_2H_2 selectivity with increasing O_2 fraction, similar to the C-based selectivities in Figure 6b. The H-based selectivity of series B (see Figure 7c) clearly indicates that a higher CH_4 fraction enhances the selectivity of H_2 and C_2H_x, and reduces the H_2O selectivity, which translates to a drop in molar H_2O formation, since the conversion of reactants is more or less constant over series B (see Figure 3b above). Figure 7d illustrates that the individual C_2H_x selectivities of series B again rise upon higher CH_4 fraction, with C_2H_2 being again the dominant component.

3.2. Analysis of the Solid Carbon Deposits. The SEM, EDX, and TEM analyses of the solid carbon samples revealed no significant differences between the samples "with O_2" and "without O_2". Therefore, we will discuss here the results of the sample "with O_2", while corresponding data for the sample "without O_2" is presented in the Supporting Information, Section S.4. However, we did observe clear macroscopic

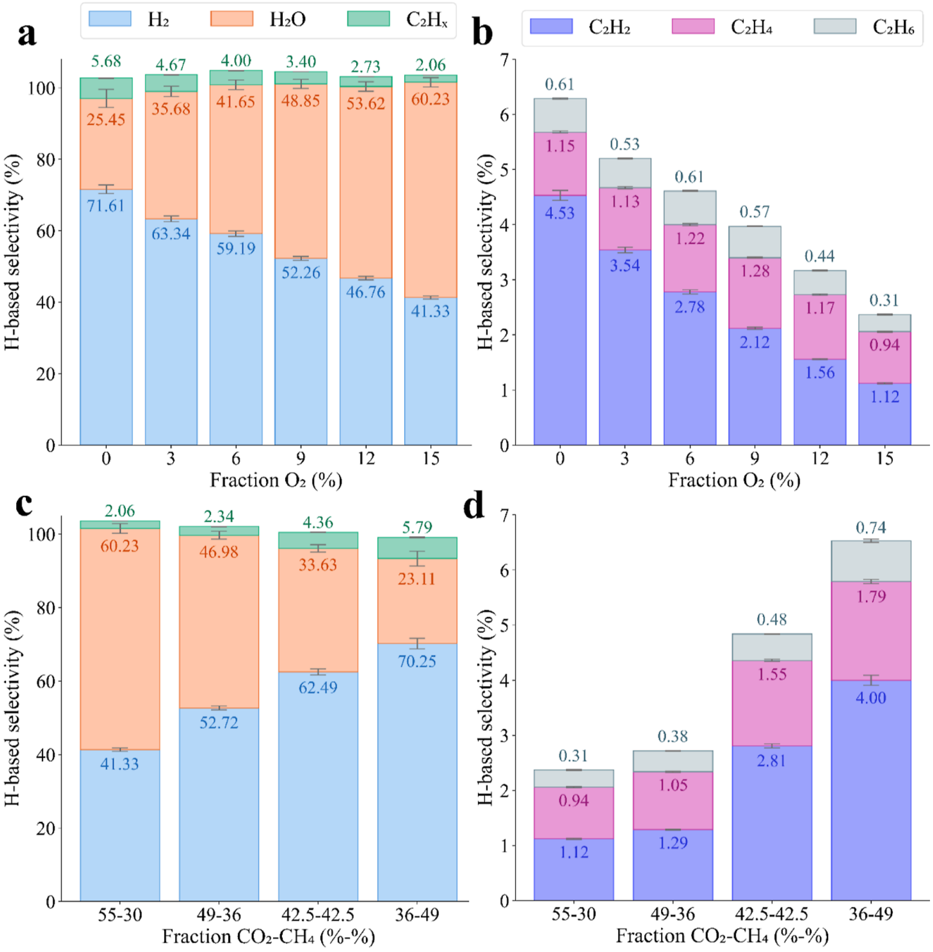

Figure 7. H-based selectivity, as a function of O_2 fraction [(a,b) series A], and CO_2/CH_4 fraction [(c,d) series B]. In (a,c) the C_2H_x compounds are combined, while in (b,d) the individual C_2H_x compounds are shown. Error bars are based on three successive experiments. As the selectivities are calculated from experimental results with small inaccuracies, the total selectivities are not perfectly equal to 1.

differences between the two experiments and corresponding samples. Most notably, the amount of solid carbon was significantly lower for the experiment with O_2 compared to the one without O_2. This makes sense, since more of the CH_4 reacts with the added O_2, limiting the amount of CH_4 that can decompose to form the solid carbon particles (see Section 3.4.3 below). This demonstrates that O_2 addition really helps to reduce solid carbon formation, which is the main aim of our work. It is however worth noting that despite the significant effect on the plasma stability, the amount of solid carbon formed was typically rather small. We were not able to collect sufficient material in a reliable way for a bulk characterization, such as thermogravimetric analysis.

An overview of the material characterization of the "with O_2" solid carbon sample is presented in Figure 8. A backscattered electron (BSE) SEM image is shown in Figure 8a, and a secondary electron (SE) SEM image of the same area is presented in Figure 8b. The BSE signal is mostly affected by the density of the sample, i.e., heavier particles will give a higher signal. The SE signal is much less sensitive to the composition of the sample, but rather reveals structural information of the surface of the material. The BSE image (Figure 8a) shows a heavy spherical particle against a light carbon background. The solid carbon itself is mostly observed as large particles or agglomerates, ranging from a few μm up to hundreds of μm. At higher magnification, the surface of the carbon appears rough, indicating it may consist of smaller structures (Figure 8b). We investigated the composition of the heavy particle in Figure 8a using EDX spectroscopy. The EDX spectrum is presented in Figure 8c and shows that the particle consists of Fe, Cr, Ni, and a small amount of Mn. This aligns very well with the composition of the stainless steel anode in the cAPGD reactor used in our work. These heavy particles were common throughout the carbon samples, and show that there is in fact electrode erosion/melting, which subsequently heavily contaminates the solid carbon formed by CH_4 in the plasma. Finally, a representative BF-TEM is shown in Figure 8d. The TEM image reveals that the material consists of graphene-like planar carbon structures, that do not have a significant ordering. This means that the material is not really amorphous, though it is also not crystalline, given the lack of long-range ordering. Based on these observations, the carbon material may be categorized as turbostratic carbon.[31,32]

While turbostratic carbon could be a valuable product, the significant contamination of the carbon with the electrode metal particles renders it much less appealing. Furthermore, the solid carbon heavily affects the plasma stability and it could accumulate downstream in the system during long operations, potentially causing blockages or posing a fire hazard. Therefore, this justifies the aim of our work to minimize the solid carbon formation, without sacrificing the overall performance.

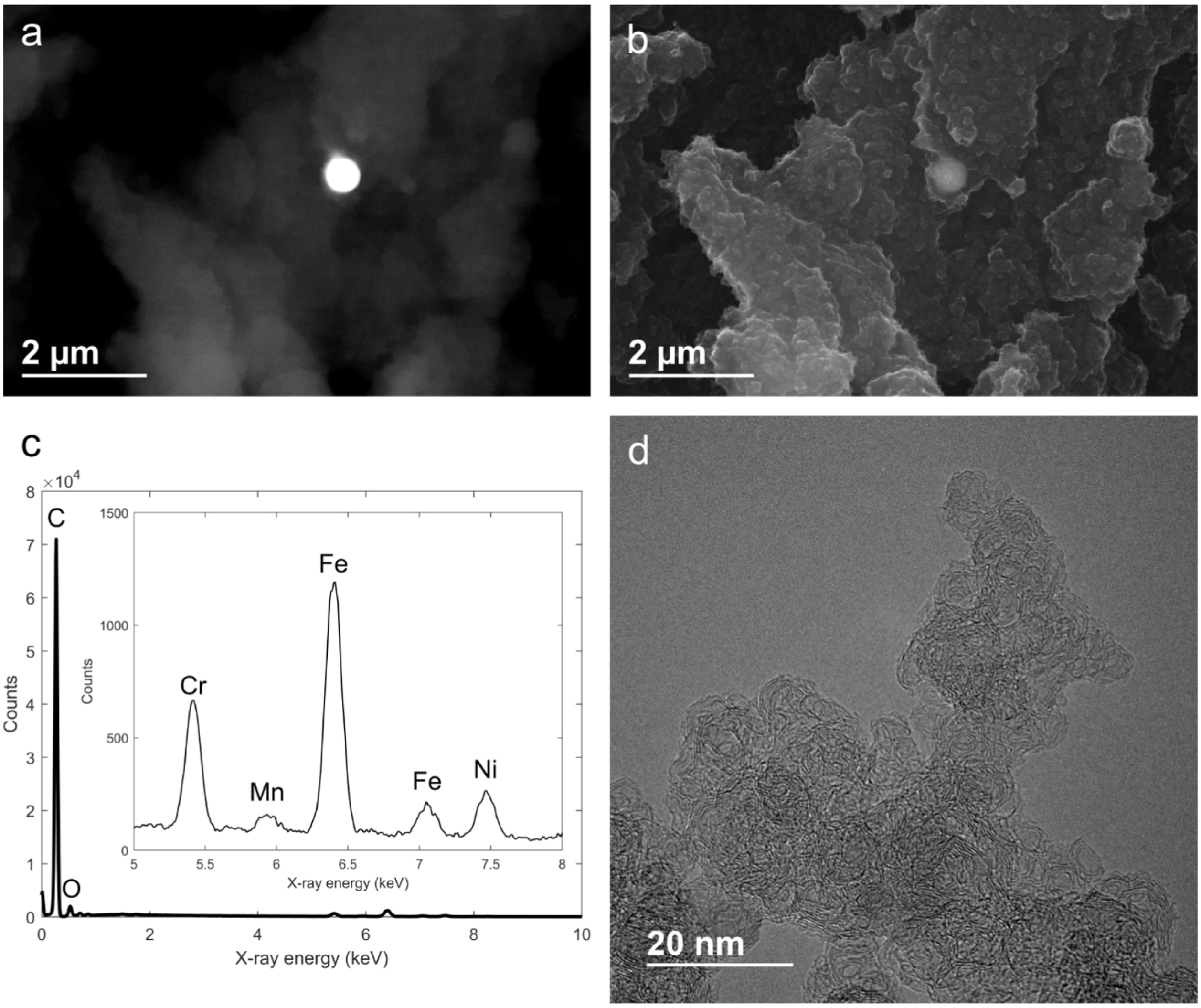

Figure 8. SEM, EDX, and TEM data for the carbon collected at the anode after an experiment with a 36:49:15 $CO_2/CH_4/O_2$ ratio. (a) BSE SEM image, highlighting a heavy, spherical particle. (b) SE SEM image of the same area as in (a), showing the microscopic structure of the carbon surrounding the heavy spherical particle. The carbon material appears to consist of a large agglomerate of smaller structures. (c) EDX spectrum of the heavy particle presented in (a), the inset shows the same spectrum but zoomed in on a relevant energy range, proving that the heavy particle is in fact stainless steel (containing Fe, Cr, Ni, and a small amount of Mn). (d) Representative BF-TEM image of the carbon material. The material consists of layers of graphene-like carbon that are not structured, indicating the material is not crystalline, but also not fully amorphous.

3.3. Benchmarking with State-of-the-Art Literature.

Some other researchers have also studied OCRM in various plasma reactors over the last decades. Table 2 compares our data with those from literature, for a spark-shade reactor,[33] an alternating current pulsed gliding arc (AC pulsed GA) reactor,[34] a spark discharge reactor,[35] a plasma-shade reactor,[36] a gliding arc plasmatron (GAP)[5] and a classical GA reactor.[37]

The results obtained in the spark-shade[33] reactor yield somewhat lower conversions, but also slightly lower energy costs, compared to our cAPGD. The authors obtained an energy cost of 1.56 eV $molecule^{-1}$ at a 39:38:23 $CO_2/CH_4/O_2$ mixing ratio, which is comparable to our value of 1.98 eV $molecule^{-1}$ at a mixing ratio of 42.5:42.5:15 (lower O_2 fraction). The lower power and higher O_2 fraction in this reactor suggest that a larger portion of the heat of the spark-shade reactor originates from the conversion of O_2. The CO_2 and CH_4 conversions at the 39:38:23 mixing ratio are 25 and 59%, respectively, i.e. much lower than our values of 50 and 74% for the 42.5:42.5:15 mixing ratio. Besides the absolute values, the results follow the same trends as in our study: a higher CH_4 and O_2 fraction simultaneously results in a lower energy cost, as well as a higher CH_4 conversion and a lower CO_2 conversion. In our work, we determined the effect of O_2 and CH_4 fraction using two separate series, but it is clear that the dominant trend in energy cost in the spark-shade reactor is similar to the trend shown by our series A, hence attributed to the change in O_2 fraction.

The CO_2 conversion in the plasma-shade[36] reactor is lower than in our experiments, but the CH_4 conversion and energy cost are similar to our data, also using similar flow rate and power. However, this paper used high O_2 fractions up to 29%, while we limited this fraction to maximum 15% as a safety precaution (see Supporting Information, Section S.1.3). At 20% O_2 fraction, the authors reached a lower CH_4 conversion and a higher energy cost than in our cAPGD. No syngas ratio was mentioned in this study.

The plasma-shade and spark-shade reactor were developed by the same group and both reactors exhibit similar conversions and energy costs as in our experiments. The major difference between these reactors and our cAPGD is the

Table 2. Comparative Study of Our Results (cAPGD) with Data for OCRM Obtained with Various Plasma Reactors in Literature

type	CO_2 (%)	CH_4 (%)	O_2 (%)	N_2 (%)	flow rate (L min^{-1})	power (W)	CO_2 conv. (%)	CH_4 conv. (%)	EC (eV $molecule^{-1}$)	H_2/CO ratio
cAPGD	55	30	15		1.04	93	47.5	87.4	1.98	0.413
	49	36	15		1.04	95	50.3	78.3	1.98	0.562
	42.5	42.5	15		1.07	94	49.5	74	1.98	0.784
spark-shade[33]	39	38	23		1.36	70	25	59	1.56[a]	0.71
	28	45	27		1.36	70	30	69	1.23[a]	0.88
	23	48	29		1.36	70	28	70	1.16[a]	1.0
	16	53	31		1.36	70	24	75	1.05[a]	1.2
	11	56	33		1.36	70	16	80	0.98[a]	1.5
AC pulsed GA[34]	32	48	20		15	280	28	52	0.60[a]	1.6
	31	46	23		15	280	25	65	0.49[a]	1.5
	29	44	27		15	280	25	77	0.42[a]	1.4
	28	42	30		15	280	33	88	0.37[a]	1.3
	27	40	33		15	280	39	95	0.35[a]	1.1
spark discharge[35]	33	56	11		0.17[a]	48	58	72	6.18[a]	1.3
	33	56	11		0.17[a]	64	67	80	7.38[a]	1.2
	32	53	15		0.18[a]	48	58	74	5.71[a]	1.2
	32	53	15		0.18[a]	64	67	80	6.94[a]	1.1
	30	50	20		0.20[a]	48	57	76	5.00[a]	1.1
	30	50	20		0.20[a]	64	68	83	6.00[a]	1.1
plasma-shade[36]	32	48	20		1.25[a]	119	36	64	2.28[a]	
	31	46	23		1.30[a]	106	34	67	2.18[a]	
	30	44	26		1.36[a]	98	31	75	2.01[a]	
	29	42	29		1.40[a]	88	35	84	1.82[a]	
GAP[5]	10	10	9	71	10	364	44	93	3.97[a]	0.60
	15	10	13	62	10	421	45	96	3.33[a]	0.68
classical GA[37]	29	29	9	33	1	100	18	23	12.57[a]	1.8
	12	28	13	47	1	100	17	27	12.57[a]	2.0
	3	25	21	51	1	100	12	46	12.61[a]	2.0

[a] Value cannot be verbatim traced in original paper; instead it was calculated using the available data/value is not present in the paper and cannot be calculated using the available data.

voltage and current profile: the spark-shade and plasma-shade operate at AC with a frequency of 95 kHz, while our cAPGD operates at DC. The voltage reaches ~4 kV at the peak of the sine wave, while the voltage in our cAPGD is kept ~10 kV. However, the AC reaches maxima of 40 mA (no root-mean-square value was provided), comparable to the 25 mA present in our cAPGD. Furthermore, the shade reactors operate using a high-voltage electrode and a rotating grounded stainless steel wire to create the desired plasma. Essentially, both these shade reactors and our cAPGD operate in the glow regime of the plasma and they produce similar results with similar SEIs. We believe that the conversion in DRM in these warm plasma reactors is due to the high plasma temperature and not due to electron reactions, as also discussed by Maerivoet et al.[20] This conclusion is supported by the fact that glow regimes, although with somewhat different electrical characteristics, lead to similar experimental results.

The spark discharge[35] shows high energy costs, but also somewhat higher conversions, which may be expected due to the low flow rate (around 0.2 L min^{-1}) and thus longer residence time, but again, exact comparison is not possible due to the different plasma reactor types. The trends, however, are similar to our work, as the energy cost drops with rising O_2 fraction. Further, a small rise in CH_4 conversion can be noted, but the difference is too little to make any firm conclusion without knowing the error values. The AC pulsed GA[34] reactor shows a very low energy cost. However, the conversion is typically also somewhat lower than in most other plasma types. Perhaps, the high flow rate used in this reactor (15 L min^{-1}) has a significant effect on the energy cost at high power when using 20−33% of O_2. Another reason could be the (much) higher O_2 fraction in the mixture. However, exact comparison is not possible, due to the different reactor setups (GA vs cAPGD). The rising conversion of CH_4 and CO_2, as well as the decreasing energy cost upon increasing O_2 fraction, do however match the trends found in our cAPGD, in spite of the quite different conditions (i.e., much higher flow rate and power, and much higher O_2 fraction). The fact that this reactor operates as an arc can yield major differences with our results. We believe further research is needed on this setup to understand the very good stated energy costs.

In earlier work from our group, a GAP[5] was investigated for CO_2 and CH_4 conversion in the presence of both O_2 and N_2. Relatively high N_2 fractions were used, to mimic industrial gas emissions, and thus the CH_4 and CO_2 fractions were quite low. The CO_2 conversion was comparable to our present study, while the CH_4 conversions was close to 100%. The slightly higher energy cost of 3.33 eV $molecule^{-1}$ can be explained by the low CO_2 and CH_4 fractions in the mixture, as part of the supplied energy is also used for undesired activation of N_2.

Finally, the classical GA[37] plasma also used N_2 in the gas mixture. It operates at similar flow rate and power as our cAPGD, but yields significantly lower CO_2 and CH_4 conversions, and a much higher energy cost of 12.57 eV molecule^{-1}, although it reaches a much more optimal syngas ratio. This is attributed to the higher CH_4/CO_2 ratio in the mixture, for which a stable plasma was enabled by the N_2 admixture. This paper demonstrates the possibility of stabilizing a high CH_4/CO_2 plasma using N_2, and thus allowing a higher syngas ratio, but at the expense of a higher energy cost.

While the arc plasmas operate at vastly different flow and power regimes, their conversion resemble the same trends. As the conversion of CH_4 reaches almost 100% for the AC Pulsed GA and the GAP the CO_2 conversion cannot surpass 50%, something that is possible and happens in the cAPGD and the spark discharge.

Overall, it is clear that in all plasma reactors, a syngas ratio above 1 is only feasible for a higher CH_4 fraction than CO_2 fraction in the mixture. Our cAPGD leads to a rather low syngas ratio compared to the other plasma reactors. Stabilizing the plasma at higher CH_4 fraction in the cAPGD will thus be necessary to increase the syngas ratio.

As mentioned above, N_2 could assist in stabilizing the plasma, allowing for a higher CH_4 fraction, albeit with increased energy cost. The spark-shade and AC pulsed GA operated at higher O_2 fraction, as well as a (somewhat) higher flow rate, although direct comparison is challenging, due to the different plasma types. Addition of H_2O vapor to the reactant mixture could also help to improve the syngas ratio, because in this case, H_2 can be produced not only from CH_4, but also from the H_2O vapor.

Apart from the syngas ratio, which clearly needs improvement in our case for most downstream processes (except Fischer–Tropsch with Fe catalyst), we can still conclude that our cAPGD is promising for the OCRM reaction, with a low energy cost (only slightly higher than for the spark-shade reactor, while the AC pulsed GA showed low values, as discussed above), and with the best CO_2 conversion of all the reactors operating around 1 L min^{-1}.

Figure 9 illustrates our best results, in terms of energy cost vs total conversion, compared to the results from literature in different types of plasma reactors for DRM, including our cAPGD. This figure is adopted from Wanten et al.,[10] who had updated figure 32 of the 2017 review paper by Snoeckx and Bogaerts.[1] Our best data corresponds to an energy cost of 1.98 eV molecule^{-1} and a total conversion of 66.7%. This energy cost is clearly lower than the efficiency target determined by Snoeckx and Bogaerts, to be competitive with classical DRM, and other emerging technologies, which was defined as 4.3 eV molecule^{-1}.[1] The total conversion is comparable to the ones obtained earlier for DRM in the same cAPGD without O_2 addition.[10] Note that Figure 9 was originally designed to compare the performance for DRM only, hence without O_2 addition; nonetheless the energy cost can be compared to other DRM plasma reactors. It is clear that stabilizing the CO_2/CH_4 plasma using O_2 is not detrimental for the energy cost of greenhouse gas conversion.

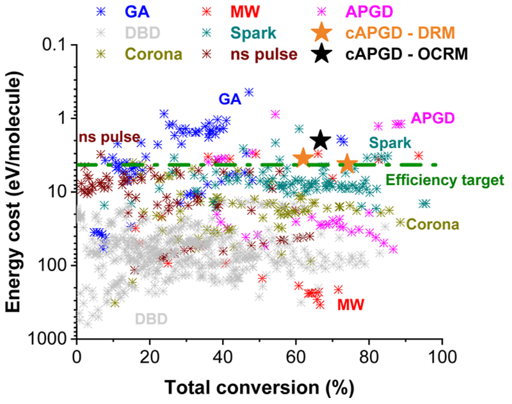

Figure 9. Overview of energy cost as a function of total conversion, based on the figure of Snoeckx and Bogaerts[1] and updated by Wanten et al.[10] Our best data point is added by the large, black asterisk. Note that the *y*-axis is reversed, with the lowest (best) values at the top. Reprinted with permission from Wanten et al.[10] Copyright 2022 Elsevier Ltd. All rights reserved.

3.4. Modeling Results and Comparison with the Experiments. We use our model to compare with the experimental trends, in terms of conversion, product output and the afterglow temperature, for model validation and to gain insights in the experimental data, especially in the underlying chemistry.

3.4.1. Conversion. Figure 10 compares the calculated and measured conversions. Series A is plotted in Figure 10a, where the experimental trend of increasing CH_4 conversion upon increasing O_2 fraction is indeed reproduced by our model. The calculated conversion of CH_4 reaches 99.9%, at the condition 55:30:15 $CO_2/CH_4/O_2$ of series A, while the experimental conversion is 87.4%. This can be explained by an overestimation of the plasma width (defining the heat source; see Section 2.4 above), and while we could fit the heat source shape to better match the experimental conversion, there would be no added value to the model. Instead, to further improve our model, we should be able to obtain the shape of the plasma from self-consistent calculations of the current conservation and Poisson equation. This will be the subject of future research.

Note that global models would provide results that better match the experiments, but this is typically accomplished by the matching of unknown experimental parameters (temperature, residence time, cooling rate,...), in other words, by fitting parameters. In contrast, in our multidimensional coupled model, we have calculated all these parameters self-consistently, without any adjustment for a better fit to the experimental data. While this obviously results in no perfect match, such multidimensional fully coupled models are definitely an improvement to gain more insight in the underlying mechanisms, at least when they are able to reproduce trends. Indeed, apart from the absolute values, the trends in CH_4 conversion are well reproduced by our model, including the largest jump in CH_4 conversion, which can be observed when going from 0 to 3% of O_2 addition for both the model and the experiment.

The trend of calculated CO_2 conversion shows somewhat weaker agreement with the experimental trend. While the experimental value gradually increases upon increasing O_2 fraction, our model shows a peak at 9% O_2 added, followed by a small drop at higher fractions. This drop is not attributed to less conversion of CO_2 in the plasma, but rather to the presence of the water–gas shift reaction after the plasma in our model, converting CO and H_2O into H_2 and CO_2. This is due to the high afterglow temperature, which is overestimated in our model, as compared to the experiments. This is further discussed in Section 3.4.3 below.

3.4.2. Product Composition. A further model validation should be based on the full composition of the outlet mixture

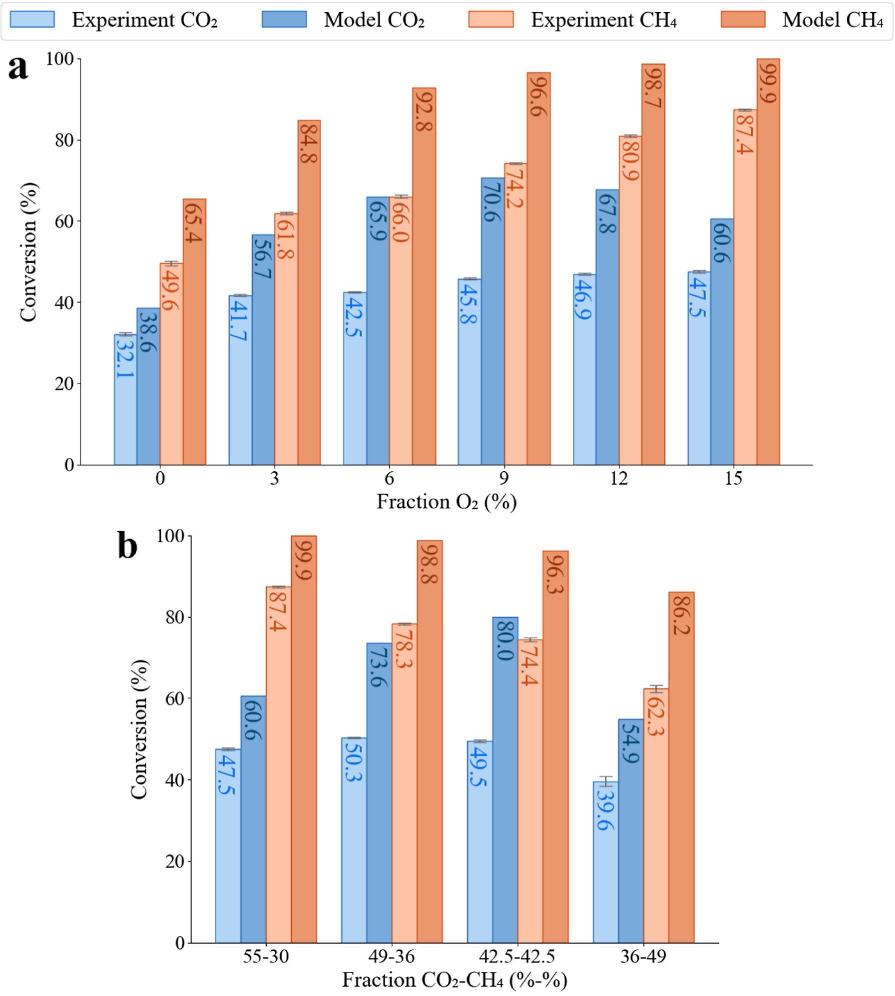

Figure 10. Experimental and modeled conversion for CO_2 and CH_4 as a function of the O_2 fraction [(a) series A] and CO_2−CH_4 fractions [(b) series B].

and not just on the conversion. Figure 11 depicts the molar composition of the gas measured in the GC and at the outlet of the model, for series A and series B. The trends in modeled and experimental CO_2 and CH_4 molar fractions match the trends in conversion shown in Figure 10 above. The water−gas shift reaction reduces the calculated CO molar fraction in conditions above 9% O_2, and it enhances the H_2 molar fraction, although the preference to form H_2O over H_2 at higher O_2 fractions results in a net decrease of the H_2 fraction upon increasing O_2 fraction, both in the model and the experiments. Furthermore, the decreasing and increasing trend of C_2H_x molar fractions in the experiments for series A and B, respectively, is somewhat exaggerated in the model. This is not only due to the approximation of the heat source (cf. above), but also due to the formation of solid C in the experiments, which could not yet be accounted for in the model. The calculated trends in CO_2, CH_4 and H_2 molar fractions in series B are similar to the experimental trends. The most important difference is the jump from condition 42.5−42.5 to 36−49 CO_2−CH_4, which can be explained by the significant power drop due to instability of the plasma, as observed in Figure 4b. The experimental trend in series B shows an increase in unconverted O_2 with increasing CH_4 fractions. We would thermodynamically expect CH_4 to exothermically react with O_2. This is not the case in the experiments, as can been seen in Figure 11b, nor is it the case in the model, where the unreacted O_2 fraction increases from 1.18×10^{-7}% at 55−30−15 (not visible in the plot as the value is too small) to 0.04% at 36−49−15. Therefore, we will analyze the temperature data below, to better understand this behavior.

3.4.3. *Afterglow Temperature.*

As described in Section 2.2, we measured the afterglow temperature 1 cm after the anode plate using a thermocouple. The calculated temperature is affected by the shape and position of the heat source, and therefore we will only compare trends, since comparing absolute values would bring no additional value, given the approximate nature of the heat source shape in the model. Figure 12a,b depict the afterglow temperature of series A and series B, respectively. The input power for all conditions (except condition 65:35:0 of series A and condition 49:36:15 of series B) is comparable, meaning that any change in temperature in the afterglow is due to a change in chemistry. Despite the difference in absolute values, the general experimental and modeled trends in series A exhibit good agreement, showing clearly that an increase in O_2 fraction leads to a higher temperature due to more exothermic reactions, as observed also in the enhanced H_2O production with increasing O_2 fraction in Figure 11a. The modeled and experimental trends of series B are also in agreement, although this cannot be explained from the thermodynamics, as mentioned before.

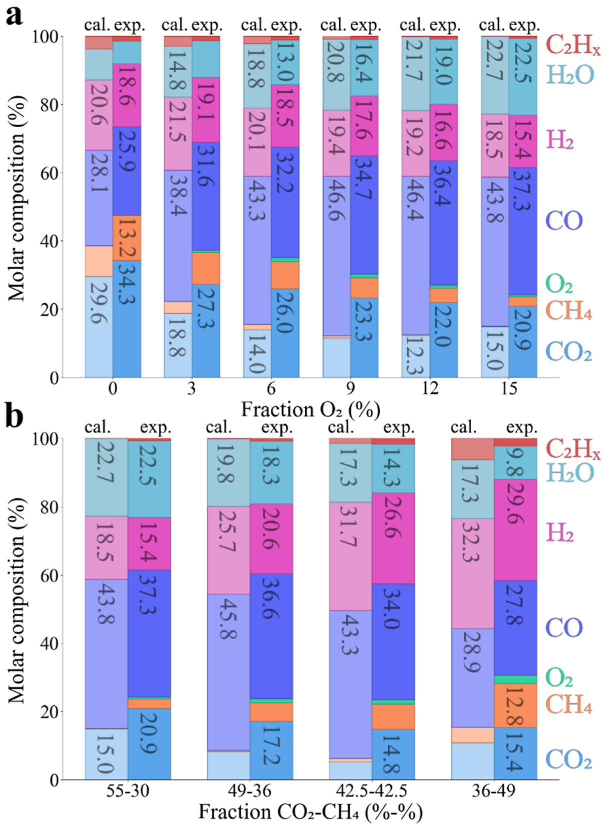

Figure 11. Molar compositions at the outlet of the experiments and the model, as a function of O_2 fraction [(a) series A] and CO_2-CH_4 fraction [(b) series B].

The drop in temperature is linked to the higher H_2 formation and the lower H_2O formation. As less O is available due to the drop in CO_2, the formation of H_2O is limited to such an extent that the edges of the plasma are not hot enough to activate the reaction between O_2 and CH_4, and this is also observed in the drop in afterglow temperature, both in the model and the experiments.

3.4.4. Multidimensional Reaction Analysis. The aforementioned temperature changes will impact the conversion, as more CO_2 and CH_4 will be converted when a larger part of the reactor has a sufficient temperature. However, the effect of O_2 on the DRM chemistry should not be neglected, and therefore, we performed a reaction analysis for conditions 65:35:0 $CO_2/CH_4/O_2$ and 55:30:15 of series A. Figure 13 shows the multidimensional reaction pathway analysis for condition 65:35:0 of series A, indicating where most of the shown species are present in the plasma, as well as the temperature profile of the plasma. Species plots in Figure 13 do not indicate how much of a species is present in a reactor, but rather where most of it resides, with the light yellow indicating a higher presence and black indicating an absence. Note that such a multidimensional reaction pathway analysis, showing not only the reaction pathways but also where in the plasma these reactions are dominant (which appears different for different reactions), is not possible with a global (0D) model, mostly used in literature for reaction pathway analysis,[10,28,38] but really requires a more-dimensional model, as used in our work.

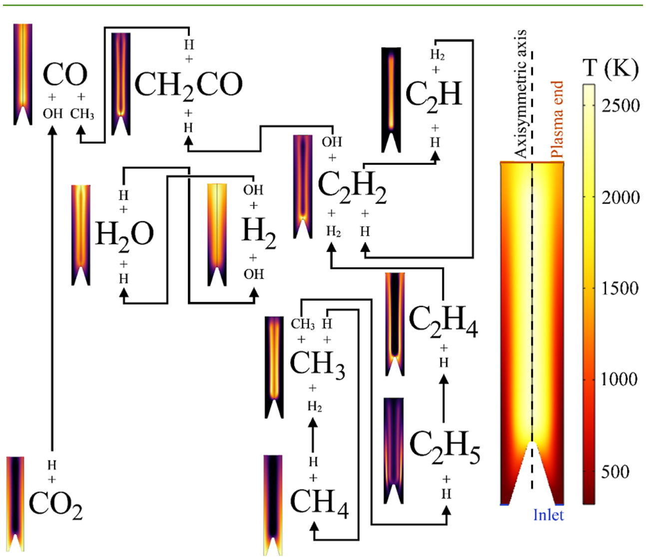

Figure 13. Multidimensional reaction pathway analysis for condition 65:35:0 $CO_2/CH_4/O_2$ of series A, indicating where most of the shown species are present in the plasma (left), with the temperature profile of the plasma shown at the right.

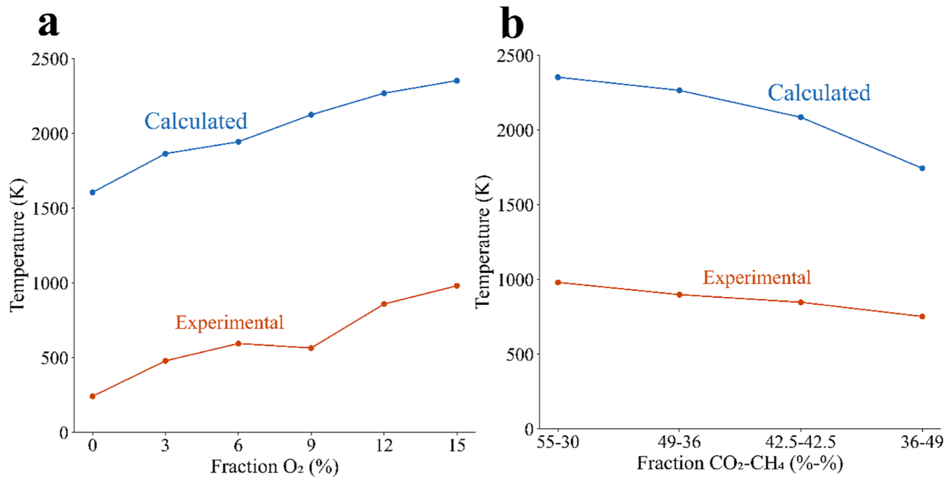

Figure 12. Experimental and modeled temperature of the afterglow, 1 cm after the anode plate, as a function of O_2 fraction [(a) series A] and CO_2-CH_4 fractions [(b) series B].

Only the species with the highest concentrations are plotted, to show a clear chemical pathway. Starting the pathway analysis from the left bottom corner, we find that almost all CO_2 conversion proceeds via reaction of CO_2 with H, to form CO and OH. The latter is an important radical for many pathways, i.e. the shift from H_2 to H_2O and vice versa (as indicated in the middle of the figure). The reaction of OH with H_2 to form H and H_2O is shown in both directions, because they are important in different regions, as indicated from the 2D species concentration profiles. The formation of H_2O from H_2 is important near the edges of the plasma, where H_2 is formed from the reaction of CH_4 and H, producing CH_3 and H_2, but it also stems from the reaction of C_2H_4 to C_2H_2 and H_2 (as also indicated in the middle-bottom part of the figure). H_2 is then again formed from H_2O in the center of the plasma. Note that the plot of H_2O shows a smaller fraction of H_2O present in the center due to this reaction. Furthermore, the production of C_2H_2 from CH_4 passes through multiple hydrocarbons. Indeed, C_2H_5 is created from CH_3, which then generates C_2H_4 closer to the center of the plasma and eventually C_2H_2 even closer to the center (see right part of the figure). We can see that additional CO is formed from reactions of C_2H_2 with, again, OH, leading to the formation of CH_2CO, which eventually decomposes with H to CH_3 and CO (left top of the figure).

Figure 14 illustrates the multidimensional reaction pathway analysis for condition 55:30:15 $CO_2/CH_4/O_2$ of series A indicating where most of the depicted species are present in the plasma, and the temperature profile of the plasma.

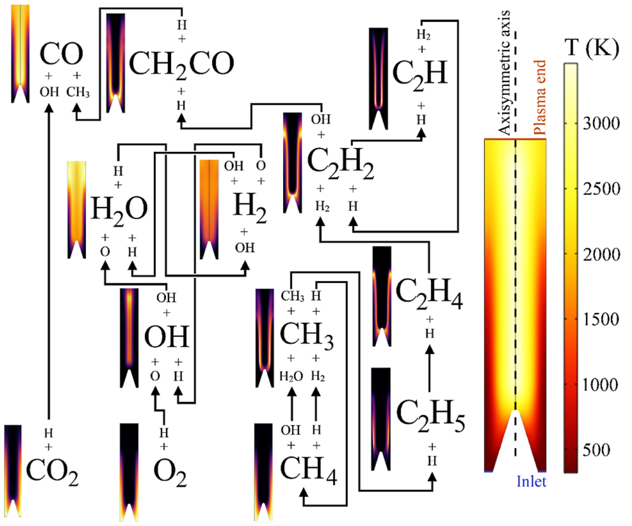

Figure 14. Multidimensional reaction pathway analysis for condition 55:30:15 $CO_2/CH_4/O_2$ of series A indicating where most of the shown species are present in the plasma (left), with the temperature profile of the plasma shown at the right.

The most pronounced difference in the chemistry compared to Figure 13 is the presence of O radicals provided by O_2, which allows for more reactions involving H_2 and H_2O to be present. The reaction of H_2 with O is an additional source for OH radicals, which can react with itself to form H_2O and O. These additional OH radicals allow for an additional reaction to destroy CH_4, as the latter now also reacts with OH radicals to form CH_3 and H_2O. The presence of C_xH_y species is now much more away from the plasma center compared to Figure 13. This is attributed to the higher temperature, forcing stronger temperature gradients.

These strong gradients result in a smaller space to be occupied by species that will react away at higher temperatures. This is also the reason why much less C_2H_2 can be found near the outlet of the model in the 15% O_2 case, which is in line with the experiments. Furthermore, as mentioned in the introduction, the Kassel mechanism[14] describes the formation of solid carbon from C_2H_2 and C_2H, both of which are more present in and near the edges of the plasma in Figure 13. Even though solid carbon particles are not taken directly into account in our model, the increased presence of its precursor according to the Kessel mechanism also indicates an increased solid carbon formation in condition 65:35:0 compared to condition 55:30:15, which is also observed in our experiments.

Furthermore, Figure 14 shows that the formation of H_2O from O_2 is mainly via the reaction of two OH radicals. This means that a rise in OH radical density, which linearly increases the removal rate of solid carbon (*rate of solid carbon removal* $\sim$ *[OH]*) results in a quadratic increase of the production rate of H_2O (*rate of* H_2O *production from* $O_2 \sim [OH]^2$). Hence, the effect of H_2O production is larger than on solid carbon removal.

Finally, we also understand that C_2H_2, and thus solid carbon, will be removed by an increase of OH radicals in the plasma, as the pathway analysis shows the production of CH_2CO in this case. Although our pathway analysis illustrates that the OH radicals are formed from the addition of O_2, we could as well consider a different source of OH radicals, e.g. H_2O. Hence, the combined conversion of CO_2 and CH_4 with H_2O addition, i.e., so-called bireforming of methane, could be of interest and has been experimentally investigated by Wanten et al.[26]

4. CONCLUSION

We investigated the effects of O_2 addition to the plasma-based conversion of CO_2 and CH_4 into syngas, i.e., so-called OCRM, in an APGD plasma reactor, by both experiments and modeling.

At an input flow rate of 1 L/min and a current of 25 mA, adding O_2 results in a more stable plasma due to the enhanced oxidation of solid carbon (formed upon CH_4 decomposition), as well as in a higher conversion of all reactants, but also in a higher selectivity toward H_2O, and thus a less valuable product output. On the other hand, at an O_2 fraction of 15%, which was the highest fraction added in our experiments for safety reasons, we could increase the CH_4 fraction beyond the value that was possible without O_2, while still having stable plasma conditions. Such higher CH_4 fractions are clearly beneficial, reaching a high conversion of all reactants, at a lower H_2O selectivity, and higher H_2 selectivity and thus a higher syngas ratio. However, too high CH_4 fractions (i.e., a $CO_2/CH_4/O_2$ mixing ratio of 36:49:15) again give rise to unstable plasma conditions due to excess solid carbon formation.

The solid carbon material formed in the plasma was found to be contaminated with stainless steel particles, originating from the electrode. The carbon itself consists of planar carbon structures without significant additional ordering, meaning it could be categorized as turbostratic carbon. However, given the contamination of the carbon with steel particles, the value of this side product appears minimal.

Modeling helps us to better understand the underlying physics and chemistry. We developed a 2D axisymmetric coupled fluid dynamics model, to calculate the conversion, product composition and gas temperature in the afterglow. Our model can match most experimental trends, although the calculated afterglow temperature is overestimated, which can be explained by the shape and position of the assumed heat source in the model. This overestimated temperature leads to (an overestimation in) the water−gas shift reaction in the afterglow. We would be able to reach better agreement by tuning the heat source in the model, but this tuning would not bring scientific added value. On the other hand, our model shows that the lower H_2O formation upon increasing the CH_4 inlet fraction at 15% O_2 can explain the lower temperature, demonstrating the value of this type of (fluid dynamics) model compared to simpler thermodynamic calculations.

Overall, we found that a $CO_2/CH_4/O_2$ mixing ratio of 42.5:42.5:15 yields the best performance, when looking at conversion, energy cost, product output, as well as plasma stability. We obtained a CO_2 and CH_4 conversion of 50 and 74%, respectively, and an energy cost of 1.98 eV molecule^{-1} (corresponding to 7.9 kJ L^{-1} and 190 kJ mol^{-1}), which is clearly below the efficiency target determined by Snoeckx and Bogaerts to be competitive with classical DRM and other emerging technologies (i.e., 4.3 eV molecule^{-1}).[1]

Mainly syngas is formed (i.e., CO and H_2), with a H_2/CO ratio of 0.8. This value is too low for direct use in methanol or Fischer−Tropsch synthesis (except when using iron catalysts). Hence, we need to make further efforts to create a more stable plasma at higher CH_4 fractions as well, in order to reach higher H_2/CO ratios, up to the order of 2. This could be achieved by adding N_2 to the gas mixture, but this is often at the expense of a higher energy cost, as demonstrated in literature, while side products may also limit the usage. Another option, supported by our modeling results, could be the addition of H_2O vapor to the plasma, which opens the way for so-called bireforming of methane

$$3CH_4\ (g) + 2H_2O\ (g) + CO_2\ (g) \rightarrow 4CO\ (g) + 8H_2\ (g) \quad \Delta H^0 = +659\ \text{kJ mol}^{-1}$$

The potential of this was recently also investigated within our group.[26]

■ ASSOCIATED CONTENT

Supporting Information

The Supporting Information is available free of charge at https://pubs.acs.org/doi/10.1021/acssuschemeng.4c04283.

Experimental setup, modeling parameters, addition SEM and TEM images and the syngas energy cost (PDF)

■ AUTHOR INFORMATION

Corresponding Authors

Stein Maerivoet − *Research Group PLASMANT, Department of Chemistry, University of Antwerp, BE-2610 Antwerp, Belgium;* orcid.org/0000-0002-1084-6697;
Email: stein.maerivoet@uantwerpen.be

Bart Wanten − *Research Group PLASMANT, Department of Chemistry, University of Antwerp, BE-2610 Antwerp, Belgium;* orcid.org/0000-0002-0802-1530;
Email: bart.wanten@uantwerpen.be

Authors

Robin De Meyer − *Research Group PLASMANT, Department of Chemistry, University of Antwerp, BE-2610 Antwerp, Belgium; Research Group EMAT, Department of Physics, University of Antwerp, 2020 Antwerp, Belgium;* orcid.org/0000-0002-2390-7233

Morgane Van Hove − *Research Group PLASMANT, Department of Chemistry, University of Antwerp, BE-2610 Antwerp, Belgium*

Senne Van Alphen − *Research Group PLASMANT, Department of Chemistry, University of Antwerp, BE-2610 Antwerp, Belgium;* orcid.org/0000-0003-0870-1453

Annemie Bogaerts − *Research Group PLASMANT, Department of Chemistry, University of Antwerp, BE-2610 Antwerp, Belgium;* orcid.org/0000-0001-9875-6460

Complete contact information is available at:
https://pubs.acs.org/10.1021/acssuschemeng.4c04283

Notes

The authors declare no competing financial interest.

■ ACKNOWLEDGMENTS

This project has received funding from the European Research Council (ERC) under the European Union's Horizon 2020 research and innovation programme (grant agreement no. 810182—SCOPE ERC Synergy project), the Excellence of Science FWO-FNRS project (FWO grant ID G0I1822N; EOS ID 40007511), the BlueApp POC project of the University of Antwerp, and through long-term structural funding (Methusalem). The computational resources and services used in this work were provided by the HPC core facility CalcUA of the Universiteit Antwerpen, and VSC (Flemish Supercomputer Center), funded by the Research Foundation—Flanders (FWO) and the Flemish Government. Finally, we thank T. Kenis and T. Breugelmans from the University of Antwerp, for performing the liquid analysis.

■ REFERENCES

(1) Snoeckx, R.; Bogaerts, A. Plasma Technology-a Novel Solution for CO 2 Conversion? *Chem. Soc. Rev.* **2017**, *46* (19), 5805−5863.

(2) Joo, O. S.; Jung, K. D.; Moon, I.; Rozovskii, A. Y.; Lin, G. I.; Han, S. H.; Uhm, S. J. Carbon Dioxide Hydrogenation To Form Methanol via a Reverse-Water-Gas-Shift Reaction (the CAMERE Process). *Ind. Eng. Chem. Res.* **1999**, *38* (5), 1808−1812.

(3) Vosloo, A. Fischer−Tropsch: A Futuristic View. *Fuel Process. Technol.* **2001**, *71* (1−3), 149−155.

(4) Hannula, I.; Kaisalo, N.; Pekka, S. Preparation of Synthesis Gas from CO2 for Fischer−Tropsch Synthesis—Comparison of Alternative Process Configurations. *J. Carbon Res.* **2020**, *6* (3), 55.

(5) Slaets, J.; Aghaei, M.; Ceulemans, S.; Van Alphen, S.; Bogaerts, A. CO 2 and CH 4 Conversion in "Real" Gas Mixtures in a Gliding Arc Plasmatron: How Do N 2 and O 2 Affect the Performance? *Green Chem.* **2020**, *22* (4), 1366−1377.

(6) Chun, D. H.; Park, J. C.; Hong, S. Y.; Lim, J. T.; Kim, C. S.; Lee, H. T.; Yang, J., II; Hong, S.; Jung, H. Highly Selective Iron-Based Fischer−Tropsch Catalysts Activated by CO 2-Containing Syngas. *J. Catal.* **2014**, *317*, 135−143.

(7) Olah, G. A. Beyond Oil and Gas: The Methanol Economy. *Angew. Chem., Int. Ed.* **2005**, *44* (18), 2636−2639.

(8) Tountas, A. A.; Peng, X.; Tavasoli, A. V.; Duchesne, P. N.; Dingle, T. L.; Dong, Y.; Hurtado, L.; Mohan, A.; Sun, W.; Ulmer, U.; Wang, L.; Wood, T. E.; Maravelias, C. T.; Sain, M. M.; Ozin, G. A. Towards Solar Methanol: Past, Present, and Future. *Adv. Sci.* **2019**, *6* (8), 1801903.

(9) Fridman, A. *Plasma Chemistry*; Cambridge University Press: Cambridge, 2008.

(10) Wanten, B.; Maerivoet, S.; Vantomme, C.; Slaets, J.; Trenchev, G.; Bogaerts, A. Dry Reforming of Methane in an Atmospheric

Pressure Glow Discharge: Confining the Plasma to Expand the Performance. *J. CO2 Util.* **2022**, *56*, 101869.

(11) Buttler, A.; Spliethoff, H. Current Status of Water Electrolysis for Energy Storage, Grid Balancing and Sector Coupling via Power-to-Gas and Power-to-Liquids: A Review. *Renewable Sustainable Energy Rev.* **2018**, *82*, 2440−2454.

(12) Li, K.; Liu, J. L.; Li, X. S.; Lian, H. Y.; Zhu, X.; Bogaerts, A.; Zhu, A. M. Novel Power-to-Syngas Concept for Plasma Catalytic Reforming Coupled with Water Electrolysis. *Chem. Eng. J.* **2018**, *353*, 297−304.

(13) Zhang, H.; Sun, Z.; Hu, Y. H. Steam Reforming of Methane: Current States of Catalyst Design and Process Upgrading. *Renewable Sustainable Energy Rev.* **2021**, *149*, 111330.

(14) Kassel, L. S. The Thermal Decomposition of Methane1. *J. Am. Chem. Soc.* **1932**, *54* (10), 3949−3961.

(15) Fedotov, A. Conversion of Methane and Carbon Dioxide on Porous Catalytic Membranes. Doctoral Dissertation, Institut National Polytechnique de Lorraine, 2009.

(16) Trenchev, G.; Nikiforov, A.; Wang, W.; Kolev, S.; Bogaerts, A. Atmospheric Pressure Glow Discharge for CO2 Conversion: Model-Based Exploration of the Optimum Reactor Configuration. *Chem. Eng. J.* **2019**, *362*, 830−841.

(17) Kashiwagura, N.; Akita, M.; Kamioka, H. Ultrasonic Study of Machinable Ceramic over Temperature Range from Room Temperature to 1000°C. *Jpn. J. Appl. Phys.* **2005**, *44* (6S), 4339.

(18) Pinhão, N.; Moura, A.; Branco, J.; Neves, J. Influence of Gas Expansion on Process Parameters in Non-Thermal Plasma Plug-Flow Reactors: A Study Applied to Dry Reforming of Methane. *Int. J. Hydrogen Energy* **2016**, *41* (22), 9245−9255.

(19) Wanten, B.; Vertongen, R.; De Meyer, R.; Bogaerts, A. Plasma-Based CO2 Conversion: How to Correctly Analyze the Performance? *J. Energy Chem.* **2023**, *86*, 180−196.

(20) Maerivoet, S.; Tsonev, I.; Slaets, J.; Reniers, F.; Bogaerts, A. Coupled Multi-Dimensional Modelling of Warm Plasmas: Application and Validation for an Atmospheric Pressure Glow Discharge in CO2/CH4/O2. *Chem. Eng. J.* **2024**, *492*, 152006.

(21) Comsol Multiphysics® 6.0. *Chemical Reaction Engineering Module User's Guide*; COMSOL AB: Stockholm, Sweden, 2023.

(22) Comsol Multiphysics® 6.0. *Heat Transfer Module User's Guide*; COMSOL AB: Stockholm, Sweden, 2023.

(23) Comsol Multiphysics® 6.0. *CFD Module User's Guide*; COMSOL AB: Stockholm, Sweden, 2023.

(24) Menter, F. R.; Kuntz, M.; Langtry, R. Ten Years of Industrial Experience with the SST Turbulence Model. In *Turbulence, Heat and Mass Transfer*; Begell House Inc., 2003; Vol. *4*, pp 625−632.

(25) Wang, Y.; Gu, M.; Zhu, Y.; Cao, L.; Zhu, B.; Wu, J.; Lin, Y.; Huang, X. A Review of the Effects of Hydrogen, Carbon Dioxide, and Water Vapor Addition on Soot Formation in Hydrocarbon Flames. *Int. J. Hydrogen Energy* **2021**, *46*, 31400−31427.

(26) Wanten, B.; Gorbanev, Y.; Bogaerts, A. Plasma-Based Conversion of Co2 And Ch4 Into Syngas: A Dive into the Effect of Adding Water. *Fuel* **2024**, *374*, 132355.

(27) Navascués, P.; Cotrino, J.; González-Elipe, A. R.; Gómez-Ramírez, A. Plasma Assisted Dry Reforming of Methane: Syngas and Hydrocarbons Formation Mechanisms. *Fuel Process. Technol.* **2023**, *248*, 107827.

(28) Biswas, A. N.; Winter, L. R.; Loenders, B.; Xie, Z.; Bogaerts, A.; Chen, J. G. Oxygenate Production from Plasma-Activated Reaction of CO2and Ethane. *ACS Energy Lett.* **2022**, *7* (1), 236−241.

(29) Yabe, T.; Sekine, Y. Methane Conversion Using Carbon Dioxide as an Oxidizing Agent: A Review. *Fuel Process. Technol.* **2018**, *181*, 187−198.

(30) Biondo, O.; van Deursen, C. F. A. M.; Hughes, A.; van de Steeg, A.; Bongers, W.; van de Sanden, M. C. M.; van Rooij, G.; Bogaerts, A. Avoiding Solid Carbon Deposition in Plasma-Based Dry Reforming of Methane. *Green Chem.* **2023**, *25* (24), 10485−10497.

(31) Long, X.; Zhang, S.; Shao, C.; Wang, B.; Wang, Y. Effects of Heat-Treatment on the Microstructure, Electromagnetic Wave Absorbing Properties, and Mechanical Properties of SiCN Fibers. *Front. Mater.* **2020**, *7*, 563891.

(32) Kowalewski, E.; Zienkiewicz-Machnik, M.; Lisovytskiy, D.; Nikiforov, K.; Matus, K.; Srebowata, A.; Sá, J. Turbostratic Carbon Supported Palladium as an Efficient Catalyst for Reductive Purification of Water from Trichloroethylene. *AIMS Mater. Sci.* **2017**, *4* (6), 1276−1288.

(33) Zhu, X.; Li, K.; Liu, J.; Li, X.; Zhu, A. Effect of CO2/CH4 Ratio on Biogas Reforming with Added O2 through an Unique Spark-Shade Plasma. *Int. J. Hydrogen Energy* **2014**, *39* (25), 13902−13908.

(34) Liu, J.; Park, H.; Chung, W.; Ahn, W.; Park, D. W. Simulated Biogas Oxidative Reforming in AC-Pulsed Gliding Arc Discharge. *Chem. Eng. J.* **2016**, *285*, 243−251.

(35) Zhu, B.; Li, X.; Liu, J.; Zhu, A. Optimized Mixed Reforming of Biogas with O2 Addition in Spark-Discharge Plasma. *Int. J. Hydrogen Energy* **2012**, *37* (22), 16916−16924.

(36) Liu, J.; Zhu, X.; Li, X.; Li, K.; Shi, C.; Zhu, A. Effect of O2/CH4 Ratio on the Optimal Specific-Energy-Input (SEI) for Oxidative Reforming of Biogas in a Plasma-Shade Reactor. *J. Energy Chem.* **2013**, *22* (5), 681−684.

(37) Thanompongchart, P.; Khongkrapan, P.; Tippayawong, N. Partial Oxidation Reforming of Simulated Biogas in Gliding Arc Discharge System. *Period. Polytech., Chem. Eng.* **2014**, *58* (1), 31−36.

(38) Morais, E.; Delikonstantis, E.; Scapinello, M.; Smith, G.; Stefanidis, G. D.; Bogaerts, A. Methane Coupling in Nanosecond Pulsed Plasmas: Correlation between Temperature and Pressure and Effects on Product Selectivity. *Chem. Eng. J.* **2023**, *462*, 142227.